Short fatigue crack growth and retained austenite in steels processed via quenching and partitioning

Garcia-Chao, Pablo; Molina-Aldareguia, Jon M.; Linke, Bernd M.; Thiessen, Richard G.; Sabirov, Ilchat

DOI
10.1016/j.matdes.2024.113228

Publication date
2024

Document Version
Final published version

Published in
Materials and Design

Materials & Design 245 (2024) 113228

Contents lists available at ScienceDirect

Materials & Design

journal homepage: www.elsevier.com/locate/matdes

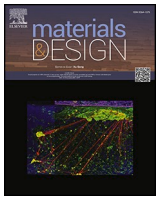

Short fatigue crack growth and retained austenite in steels processed via quenching and partitioning

Pablo Garcia-Chao [a,d,*], Jon M. Molina-Aldareguia [b,a], Bernd M. Linke [c], Richard G. Thiessen [c], Ilchat Sabirov [a]

[a] IMDEA Materials Institute, C/Eric Kandel 2, Tecnogetafe, Getafe, 28906 Madrid, Spain
[b] Department of Mechanical Engineering, Universidad Politecnica de Madrid, C/Jose Gutierrez Abascal 2, 28006 Madrid, Spain
[c] Thyssenkrupp Steel Europe AG, Kaiser-Wilhelm-Strasse 100, 47166 Duisburg, Germany
[d] Department of Materials Science and Engineering, Delft University of Technology, Mekelweg 2, 2628 CD Delft, The Netherlands

ARTICLE INFO

Keywords:
Short cracks
Retained austenite
Steels
Fatigue crack growth
Electron backscatter diffraction

ABSTRACT

Previous research has consistently found that introducing metastable retained austenite (RA) as a second phase retards the failure of steel under fatigue. However, the reasons for this benefit are not understood. Accordingly, the properties of RA most advantageous to resist fatigue are not known. Within this context, this paper examines the interaction between second-phase RA and short fatigue crack growth in a steel processed via quenching and partitioning, using quasi *in situ* electron backscatter diffraction experiments. Results show that most RA transforms into martensite under the plastic strain surrounding the crack. They also reveal various mechanisms whereby RA transformation delays short fatigue crack propagation; transformation-induced crack closure (TICC), crack deflection and branching, and roughness-induced crack closure (RICC). Crack deflection and branching are driven by a tendency of cracks to propagate towards transformed RA, which is against the previous assumptions in the literature. Furthermore, the impact of crack deflection/branching on retardation is more powerful than that of TICC acting alone. Microstructures including second-phase RA should avoid RA-lean areas and promote elongated RA grains, with relatively large size, and major axis normal to the preferential crack growth direction. Untransformed RA within the plastic zone (i.e. overstabilized) does not contribute to crack retardation.

1. Introduction

Introducing retained austenite (RA) as a second phase is a common strategy to enhance the mechanical properties of novel steel grades. This approach was first employed in transformation-induced plasticity (TRIP) steels, which are now extensively used in the automotive industry. Since then, other steel types comprising significant volume fractions of RA have been developed. These include carbide-free bainitic (CFB), quenching-and-partitioning (Q&P) and medium-manganese (medium-Mn) steels [1,2]. CFB and Q&P steels are already widely commercially available [2]. Medium-Mn steels exhibit promising results, but are still in a development stage [2].

Among the different mechanical properties, the role of second-phase RA in enhancing ductility and formability is well-established [1,3], and ascribed to the so-called TRIP effect. By this effect, RA grains transform into martensite under plastic strain, which provides a mechanical driving force for the transformation [3]. Second-phase strengthening owing to the newly-formed martensite leads to high work hardening rates, which retard the onset of failure [1,3,4].

Accordingly, studies have also been carried out on the effect of second-phase RA on fatigue performance. A beneficial effect has generally been observed for all relevant steel types: TRIP [5–11], CFB [12–19], Q&P [20–22] and medium-Mn steels [23–26]. Furthermore, the improvement has been reported under both high-cycle fatigue (HCF) [5–9,12,14,19–24] and low-cycle fatigue (LCF) [7,9–11,13,15–18,23,25,26]. This benefit has been related to the transformation of RA into martensite during fatigue crack propagation, for both LCF and HCF [6,12–14,18,19,22–24,28–30]. Occurrence of this transformation has been suggested by lower RA volume fractions measured around fatigue fracture surfaces [22,24,28–31], and fresh martensite observed near fatigue cracks [14,30]. The mechanical driving force would be contributed by the plastic strain surrounding the

* Corresponding author.
E-mail address: p.garciachao@tudelft.nl (P. Garcia-Chao).

https://doi.org/10.1016/j.matdes.2024.113228
Received 24 April 2024; Received in revised form 29 July 2024; Accepted 1 August 2024
Available online 5 August 2024

crack [30,31]. However, unlike the reason for the enhanced formability, the mechanisms whereby RA transformation ahead of fatigue cracks can retard their growth are not well-understood.

On the one hand, some authors have referred to transformation-induced crack closure (TICC) [14,23,28,31,32]. The volume expansion accompanying the transformation of RA (face-centered cubic) into martensite (body-centered cubic or tetragonal) gives rise to a compressive stress field around the transformed RA [33]. This would lead to a relaxation of the stress around the crack, which would retard its further growth. On the other hand, other authors have suggested that RA transformation may lead to crack branching and deflection [6,24,29]. A mechanism for such behavior was proposed by Huo and Gao [29]. In their view, crack growth after closure via TICC could only be resumed by a new branch formed elsewhere along the crack path. This branch would lie at 45° to the main crack, following the slip plane of maximum dislocation accumulation in the plastic zone (and this leading to crack deflection) [29]. Nevertheless, direct evidence of whether RA transformation effectively leads to TICC and crack branching/deflection has not been given. Furthermore, the relative contributions to the retardation of TICC acting alone and crack branching/deflection are unknown. This is due to former studies relying on post-mortem observations only: due to its transformation into martensite, the interactions between RA and fatigue cracks cannot be examined unless RA grains are identified before crack passage. Although the resultant fresh martensite can be observed, this phase is also a product of the final cooling in the thermo-mechanical processing of RA-containing steels [1,14,29,30,34]. Hence, it cannot be ascertained whether any fresh martensite resulted from RA transformation upon crack passage, or was already present in the initial microstructure.

Apart from this, fatigue crack growth is customarily divided into two stages depending on crack length: short and long crack growth [35]. Short crack growth is further subdivided into microstructurally short crack (MSC) and physically short crack (PSC) growth. In MSC growth, propagation is strongly influenced by the microstructure: microstructural barriers like grain boundaries can have a far-reaching effect in delaying or arresting the crack. In PSC growth, propagation becomes decreasingly influenced by microstructure. Finally, the crack reaches the long stage, when growth escapes the microstructural constraints. Therefore, the improvement of fatigue performance by second-phase RA is more likely due to a retardation of short fatigue crack growth.

Within this context, the interactions between second-phase RA and short fatigue crack growth are here examined for a Q&P steel, via electron backscatter diffraction (EBSD) in quasi *in situ* experiments. By these means, EBSD analysis is conducted in the same area before and after crack passage. Hence, RA grains can be identified before the corresponding area is included in the plastic zone ahead of the crack tip, avoiding the limitations of past studies. This makes it possible to elucidate whether short fatigue crack growth is effectively delayed by second-phase RA and, in that case, by which mechanisms. Such an approach also enables the identification of the properties of the RA grains most suitable to fatigue. The outcome of this study can thus serve as input to the future design of microstructures including RA so that fatigue performance is considered, in addition to other mechanical properties. This information becomes more relevant nowadays, with the advent of laser-based treatments whereby RA patterns with specific size, morphology and orientation can be easily applied to steels with multi-phase microstructures [36,37]. Characterization is complemented by post-mortem transmission electron microscopy (TEM).

2. Material and methods

2.1. Material

The chemical composition of the Q&P steel is presented in Table 1. A cold rolled 1.5 mm sheet was fully austenitized at 870 °C for 100 s and then quenched to a temperature (QT) of 280 °C to achieve a microstructure consisting of martensite and austenite. Subsequently, the material was reheated to a partitioning temperature (PT) of 400 °C and held isothermally for a partitioning time (Pt) of 50 s. Finally, it was quenched to room temperature. These partitioning conditions ensured a considerable partitioning of carbon from martensite to austenite, avoiding significant tempering of the martensite. The final microstructure consisted of a matrix of tempered martensite, with RA as a second phase, and a small fraction of fresh martensite (Fig. 1).

Table 1
Chemical composition of the steel studied (wt. pct).

Fe	C	Si	Mn	Al	Cr	P	N
Bal.	0.2	1.25	2.4	0.02	0.025	0.01	0.002

Quantitative characterization of the RA grains in the microstructure can be seen in Table 2, as performed by EBSD. The average volume fraction of RA was 5.3 %, with an average RA grain size of 0.32 ± 0.19 μm. The largest RA size detected was 1.45 μm, and aspect ratios of the RA grains ranged from 1 to 11.5. In this sense, ~50 % of RA grains had elongated shape, i.e. aspect ratios higher than 2. Elongated and equiaxed RA grains did not show significant differences in terms of size (Table 2). For elongated RA grains, all angles between the major grain axis and the specimen longitudinal axis were present with roughly equal probability. The average local volume fraction of fresh martensite was 1.3 %. The average grain size of martensite was 1.1 ± 1.7 μm, with an average parent austenite grain size (PAGS) of 3.9 ± 0.8 μm. The RA volume fraction as measured by X-ray diffraction was 10.3 % [38].

Uniaxial tensile testing of the Q&P treated material revealed a yield strength of 988 MPa, an ultimate tensile strength of 1203 MPa, and a total elongation of 10.8 % [38].

2.2. Fatigue tests

RA identification by EBSD before passage of the short fatigue cracks required scanning the area where the cracks would grow before they formed. Yet, for a specimen with a homogeneous microstructure, the initiation points of the cracks are in principle unknown. At the same time, the small RA size enforced a relatively small step size in the EBSD acquisition (55 nm), making it impossible to scan large areas. Therefore, crack initiation was localized by introducing a notch in the fatigue specimens.

The dimensions of the notched tensile specimens used in the fatigue tests are given in Fig. 2***(a)***. The specimens were manufactured by electrical discharge machining, with the longitudinal direction parallel to the sheet rolling direction. After machining, the specimens were ground and polished. The notch was introduced after the last polishing step using a wire cutting machine. This process produced a protruding burr parallel to specimen thickness, which hindered EBSD acquisition after

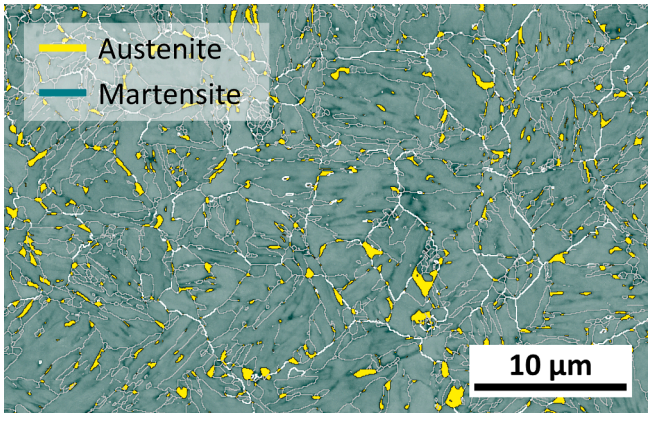

Fig.1. EBSD map corresponding to the initial microstructure.

Table 2
Quantitative characterization of the retained austenite grains in the initial microstructure.

Type of Grains	Volume Fraction	Number Fraction	Diameter (μm)	Aspect Ratio
All RA Grains	5.3 %	100 %	0.32 ± 0.19	2.07 ± 1.15
Equiaxed RA Grains (Aspect Ratio < 2)	2.3 %	47 %	0.28 ± 0.16	1.53 ± 0.26
Elongated RA Grains (Aspect Ratio ≥ 2)	3.2 %	53 %	0.34 ± 0.19	3.08 ± 1.15

the specimen was tilted to 70° in the scanning electron microscope (SEM). Hence, the burr was eliminated at the wire cutting machine by gradually increasing the load at the end of the notching process. The notches introduced had a width of approximately 90 μm and lengths ranging between 150 and 250 μm. Such notches had a stress concentration effect during the fatigue tests. Particularly, the stress concentration due to a notch of similar dimensions was evaluated via finite element analysis by Christodoulou *et al.*, for a TRIP steel [9]. For a similar yield strength-stress applied ratio as in our experiments, calculations suggested a stress around the notch (radius > 250 μm) higher than yield strength, i.e. consistent with LCF [9].

The fatigue tests were performed in an Instron 8802 testing machine, with nominal stress amplitude of 450 MPa (relative to the unnotched cross-section), R-stress ratio of 0 and frequency of 10 Hz.

EBSD was carried out ahead of the notch before fatigue testing (Fig. 2 ***(b)***) to encompass the area of the short crack growth. A distance of at least 5 μm was always left between notch tip and the EBSD scans. During fatigue testing, fatigue crack initiation and length were monitored ex-situ at defined cycle intervals with an optical microscope. When specific events upon fatigue crack growth were detected, characterization was completed by SEM imaging and EBSD in the same area scanned before the fatigue test (Fig. 2***(b)***). SEM imaging was used to observe the crack path. EBSD was performed to assess the underlying microstructure, including the presence of RA. For one of the specimens, EBSD was also performed after testing (500 cycles), but before fatigue crack initiation. No significant transformation of RA (< 5 %) was observed to have been induced by the notch, compared to the microstructure before testing. The increase in mean kernel average misorientation, which correlates with the extent of plastic strain, was consistent with a strain of 1.3 % under monotonic tensile testing (0.9 to 1.0° [39]).

2.3. Microstructural characterization

The specimens were prepared for microstructural characterization with EBSD by grinding and polishing following standard metallographic techniques. A mirror-like surface was achieved by performing final polishing with oxide polishing suspension (OP-U) for 10 min. The EBSD analysis was conducted using a FEI Helios NanoLab 600i microscope. The microscope was equipped with a NordlysNano detector controlled by the aZtec Oxford Instruments Nanoanalysis (version 2.4®) software. The data acquisition was carried out at an accelerating voltage of 18 kV, a working distance of 8 mm, a tilt angle of 70°, and a step size of 55 nm. For SEM imaging, the same microscope was utilized, operating at an accelerating voltage of 18 kV. SEM images were captured from the areas of interest. In all the images shown, the direction of loading is aligned with the horizontal direction of paper.

The orientation data obtained were post-processed using the HKL post-processing Oxford Instruments Nanotechnology (version 5.1©) software. RA and martensite grains were detected as having face-centered and body-centered cubic crystal structures, respectively. In the maps shown, the white lines account for parent austenite grain boundaries (PAGBs). These were identified as martensite boundaries with misorientations between 21° and 47° [40]. The black lines correspond to phase boundaries, and the grey lines to boundaries between grains of the same phase, with misorientation larger than 5°. The EBSD maps show band contrast, with RA superimposed and colored following the inverse pole figure of the sheet normal direction. RA and martensite grains were constructed for a minimum boundary misorientation of 15°, excluding those formed by less than four pixels. Grain size is given as equivalent grain diameter. The PAGS was measured by linear intersection, for the identified PAGBs. Grain aspect ratios were obtained as the ratio between the lengths of the major and minor axes of the ellipse approximating grain shape. Grain inclination to the main direction of crack growth was derived as the angle between the major axis of the ellipse above, and the normal direction to the longitudinal specimen axis. Slip plane identification and Schmid factor analysis from the EBSD maps were carried out with the OIM Analysis v8.6 software. Crack paths were associated with {110} slip planes if aligned with a tolerance of 5°. In those cases, the corresponding slip plane traces are superimposed in the EBSD maps in purple, with the slip system with the highest Schmid factor (SF) also indicated. Short fatigue crack growth along {110} slip planes has been previously identified for ferrite in steel [41].

In order to prepare cross-sectional transmission electron microscopy (TEM) lamellae for specimen after fatigue testing, a focused ion beam (FIB) technique was employed using a FIB-FEGSEM dual-beam microscope (Helios NanoLab 600i, FEI). The TEM sample was extracted from a region containing the fatigue crack. Subsequently, TEM characterization was carried out using a FEG S/TEM microscope (Talos F200X, FEI) operating at 200 kV.

3. Results

In all the specimens analyzed, fatigue cracks were first detected after a few hundreds of cycles. This behavior is consistent with failure under

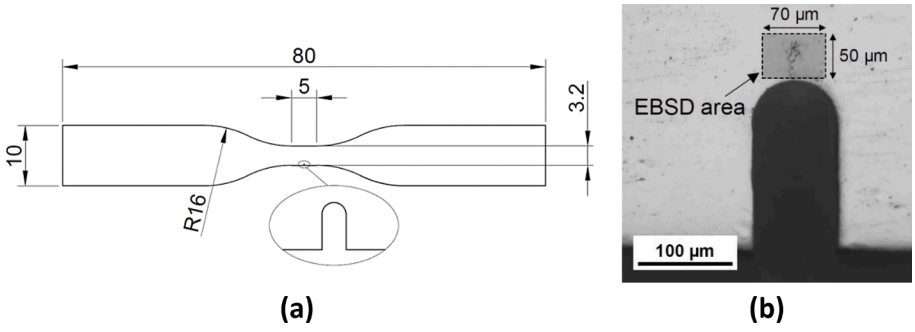

Fig.2. (a) Geometry of the fatigue specimens (dimensions in mm). (b) Example of notch geometry and area scanned with EBSD for Crack 3.

LCF. Cracks always originated at the edge of the notch and close to the notch tip (within a distance of 15 μm, as measured perpendicularly to the longitudinal axis of the notch). In most cases, multiple cracks appeared in one specimen, but only one of them persisted to ultimately cause failure. When multiple cracks were present, the first crack always appeared at the notch tip. As shown in ***Sections 3.1 and 3.2***, growth of the short cracks often occurred transgranularly, normal to the stress applied. Crack growth perpendicular to the principal tensile stress is energetically favored [42].

About RA, only negligible transformation into martensite ahead of the notch was observed by EBSD before crack initiation (< 5 % after 500 cycles, with no crack). This means that the cyclic loading preceding crack formation did not induce RA transformation. Hence, the transformation effects discussed below can be directly ascribed to the plastic strain zone at the crack tip. The radius inside which RA transformation was observed was significantly larger than the PAGS (e.g., ~25 μm for a crack length of ~20 μm). Most RA inside the plastic zone did transform into martensite, with exceptions highlighted when presenting the results below. In this sense, the stability of RA grains is controlled by the interplay of numerous factors (content of austenite-stabilizing elements, grain size and morphology, crystallographic orientation, neighborhood, etc. [3]). For this Q&P grade, some RA grains still existed in the microstructure after formability testing, reaching a plastic strain of 65.8 % [38].

The results are divided into three subsections. The first two show results corresponding to the quasi *in situ* EBSD analysis: in the first of them, a propagating and a non-propagating crack corresponding to the same specimen are compared; the second one follows a propagating crack for a larger number of cycles in another specimen. Finally, the third subsection displays using TEM the behavior of the RA grains that could not be captured with EBSD.

3.1. Propagating vs non-propagating cracks

One of the specimens analyzed showed two cracks after 900 cycles (Fig. 3***(a)***). Crack 2 was first observed after 400 cycles, while Crack 1 was already present after 300 cycles (Fig. 3***(b)***). From 400 to 700 cycles, Crack 2 grew steadily from 4 to 12 μm, while Crack 1 experienced marginal growth only. After 700 cycles, Crack 2 did not grow any further before specimen fracture (non-propagating crack). On the other hand, Crack 1 continued growing until eventually leading to ultimate specimen failure. The microstructures corresponding to the growth of Crack 1 and 2 in the area encompassed by blue dashed lines in Fig. 3***(b)*** are shown in Fig. 4 and Fig. 5, respectively.

Propagation of Crack 1 beyond the final length reached by Crack 2 occurred between 700 and 900 cycles. In that stage, growth of Crack 1 mainly occurred inside a single parent austenite grain (PAG) (Fig. 4***(b)***). The initial local RA volume fraction in this PAG was 3.0 %. All RA inside the PAG transformed due to the crack, except for a RA grain fragment at the furthest corner from the crack path (red arrow in Fig. 4***(c)***). Crack growth in this region was always roughly perpendicular to the load applied, albeit following a zigzag path. The changes of direction were subtle, and appeared when the crack crossed the PAGB (A in Fig. 4***(b)***), and other martensite boundaries (e.g., B-D in Fig. 4***(b)***). Similar zigzag paths have been reported in other steels with martensite matrix, and related to the different crystallographic orientations of martensite blocks [28]. No interaction between the crack and the transformed RA grains in this PAG occurred, with the exception of grain E (Fig. 4***(b)***). The crack slightly deviated in front of that grain, which represented its end point after 900 cycles. Yet, E was approximately aligned with the crack normal to the load applied, so the change of direction was not significant.

Similarly, the path of Crack 2 between 500 and 700 cycles (i.e. just before its arrest) included two branches, comprising three PAGs (Fig. 5***(b)***). The combined initial RA local volume fraction in these PAGs was 4.6 %. Only some RA grain fragments remained untransformed, lying at the furthest positions from the crack path (Fig. 5***(c)***). When entering this region, crack growth was normal to the tensile load, traversing a PAG where RA grains were elongated and had major axis parallel to crack path (A in Fig. 5***(b)***). Afterwards, the crack strongly deviated towards transformed RA grain B. B was also elongated, but its major axis was roughly normal to crack path. After B, the crack propagated at an angle of ~35° to the load applied, towards another transformed RA grain (C in Fig. 5***(b)***). Both B and C lied along the same martensite boundary (presumably, a PAGB). However, crack path between B and C did not follow the boundary. C was the arrest point of this branch. Starting at B, an additional branch developed, ending at another transformed RA grain (D in Fig. 5***(b)***). This grain belonged to a different PAG, as shown by its different crystallographic orientation (blue in the IPF coloring of Fig. 5***(b)***, against red for the RA grains around B-C).

3.2. Evolution of a propagating crack

The complex branching behavior of a propagating crack observed in another specimen (Crack 3, which would lead to ultimate specimen failure) was also analyzed. After 1650 cycles, Crack 3 exhibited two main branches, together with a Secondary Branch formed in its early growth stages (Fig. 6***(a)***). Crack 3 was first detected after 650 cycles (Fig. 6***(b)***). In the following 350 cycles, crack growth alternatively underwent stages of quick, slow, then quick growth again: ~0.1 μm/cycle at 650–750 and 900–1000 cycles, and ~0.03 μm/cycle between 750 and 900 cycles. The Secondary Branch developed between 750 and 900 cycles. Afterwards, Crack 3 did not further grow between 1000 and 1150 cycles (partial crack arrest). Crack growth was resumed by the development of Branch 1 between 1150 and 1450 cycles (~0.07 μm/cycle). Branch 1 arrested at an overall crack length of ~42 μm. Subsequently, Branch 2 developed (~0.06 μm/cycle), stopping after 1550 cycles and overall crack length of ~40 μm. Arrest of Branch 2 was followed by the formation of Branch 3, starting from an intermediate point of Branch 2.

Just before formation of the Secondary Branch, the crack propagated

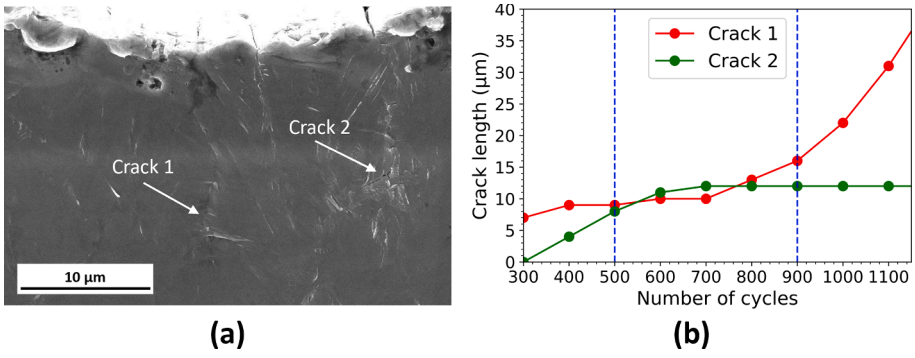

Fig.3. Cracks 1 and 2: (a) SEM image after 900 cycles, and (b) crack length against number of cycles.

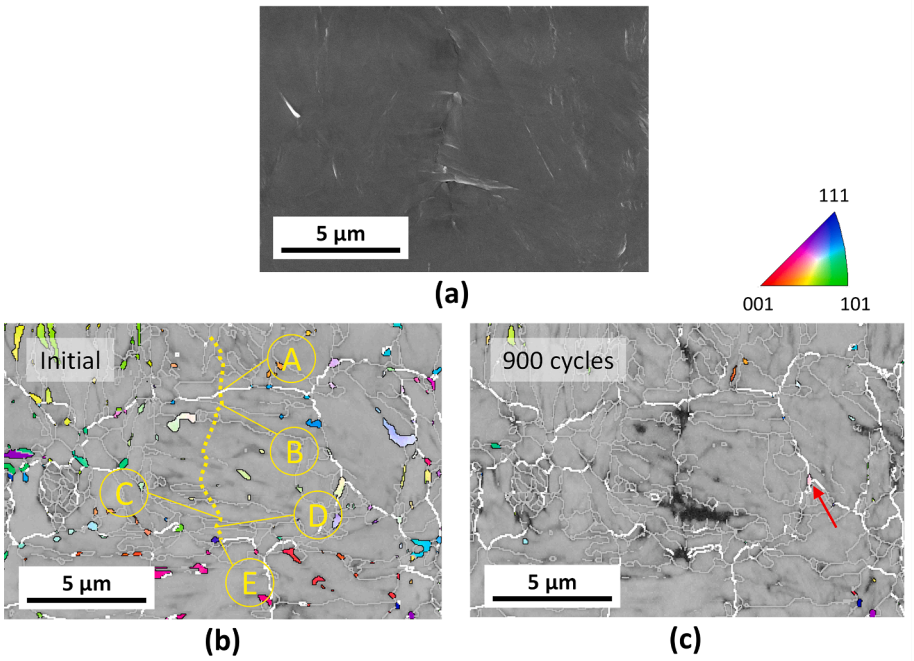

Fig.4. Crack 1: (a) SEM image, and EBSD maps of the same area (b) before testing and (c) after 900 cycles. The dotted yellow line indicates crack path. (For interpretation of the references to colour in this figure legend, the reader is referred to the web version of this article.)

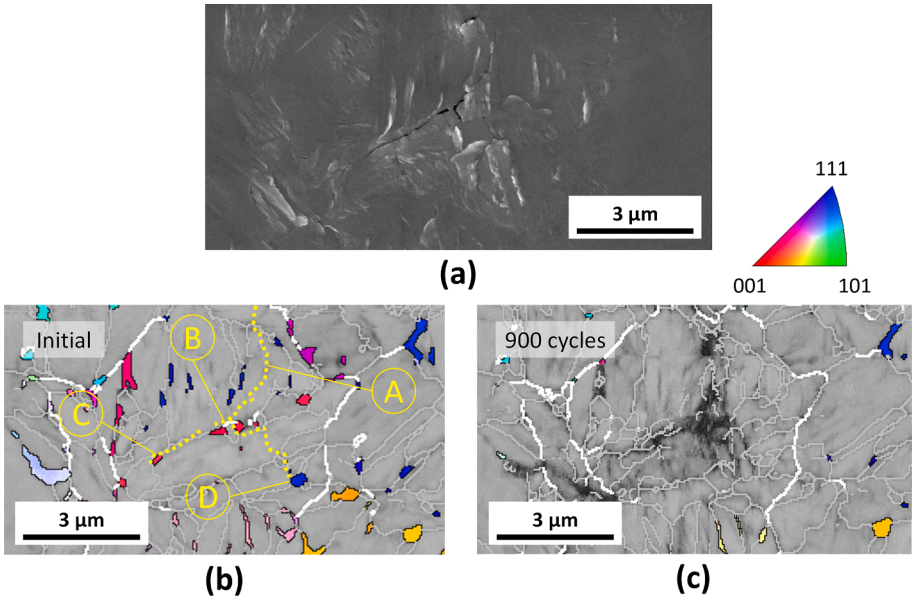

Fig.5. Crack 2: (a) SEM image, and EBSD maps of the same area (b) before testing and (c) after 900 cycles. The dotted yellow line indicates crack path. (For interpretation of the references to colour in this figure legend, the reader is referred to the web version of this article.)

perpendicularly to the load applied (Fig. 7***(a)***). The crack then deflected towards the transformed RA grain labelled as A, forming ~20° to the load applied (Fig. 7***(a)***). The area around grain A is shown with greater detail in Fig. 8. Growth resumed from another point around the interface of A, and the resultant crack propagated up to a further transformed RA grain (B in Fig. 8). Only the portion of B in direct contact with the crack transformed into martensite (Fig. 7***(b)***). After B, the crack grew parallel to the load applied towards transformed RA grain C (Fig. 8). Later, the crack became normal to the load, but changed direction once again towards the RA grain labelled as D (Fig. 8). D was part of a RA grain cluster (Fig. 7***(a)***), which fully transformed into martensite. Two branches then started at D, each growing up to a transformed RA grain: the first one following a martensite boundary (DE in Fig. 7***(a)***), and the second one the (1 1 0) slip plane of the corresponding martensite grain (DF in Fig. 7 ***(a)***). The Secondary Branch did not propagate any further. The slip system (1 1 0)[-11–1] in DF had a Schmid factor (SF) of ~0.41. Studies on short fatigue crack growth have repeatedly reported propagation along slip planes with high Schmid factors [41,42].

After the arrest of the Secondary Branch, the crack resumed growth transgranularly, across a martensite grain (G in Fig. 7***(a)***). Growth in G followed the (1–10) slip plane in that grain, for which (1–10)[11–1] was the slip system with the highest Schmid factor (SF ≈ 0.49). The crack changed direction once again (H in Fig. 7***(a)***) to follow a martensite boundary decorated with three transformed RA grains (H-M in Fig. 7

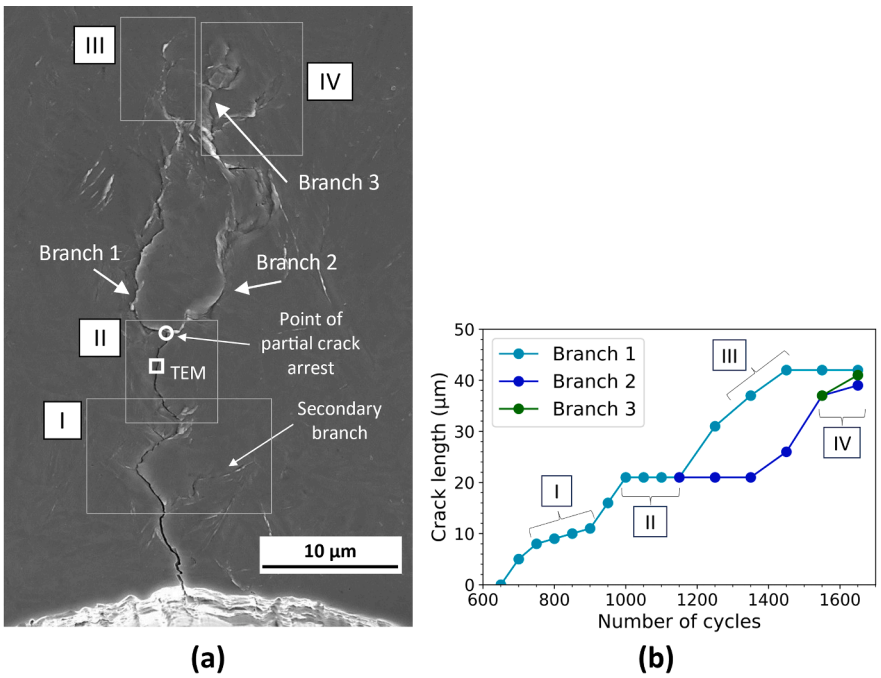

Fig.6. Crack 3: (a) SEM image after 1650 cycles, and (b) crack length against number of cycles.

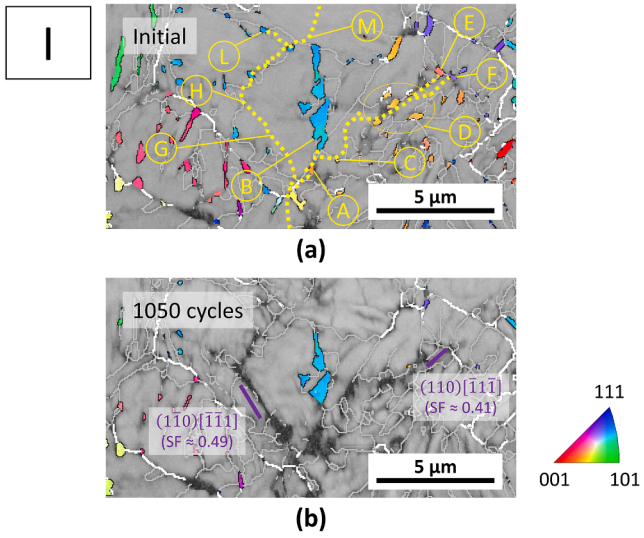

Fig.7. Area I of Crack 3: EBSD maps of the same area (a) before testing and (b) after 1050 cycles. The dotted yellow line indicates crack path. The purple lines account for slip plane traces, for which the slip system of highest Schmid factor (SF) is given. (For interpretation of the references to colour in this figure legend, the reader is referred to the web version of this article.)

(a)). This section is more clearly seen in the enlarged detail in Fig. 9: the crack followed all three RA grains (I, J and K), but following a path different from the boundary. After the latter was exhausted, crack path recovered a direction roughly normal to the tensile load at M (Fig. 9). A secondary micro-crack formed between one of the RA grains at the martensite boundary (K), and another transformed RA grain lying at a short distance (~2 µm, L in Fig. 9).

Before entering the PAG where the partial arrest took place, Crack 3 bifurcated. One branch travelled towards the interface of an adjacent transformed RA grain (A in Fig. 10***(a)***), then continued up to another one (B in Fig. 10***(a)***). This branch developed a further sub-branch, again ending at a partially transformed RA grain (C in Fig. 10***(a)***). Only the closest portion of C to the crack tip transformed. The other branch entered the PAG of the partial arrest, and became the main crack. This branch exhibited a minor deflection in front of a transformed RA grain (D in Fig. 10***(a)***), then followed the preferential direction up to the partial arrest. All RA grains around this crack path segment transformed, except for one especially close to the crack (red arrow in Fig. 10***(b)***). The partial arrest occurred at the interface of a transformed RA grain (E in Fig. 10***(a)***). This grain was elongated, with major axis normal to crack path. The crack underwent a minor deflection in front of E. After the partial arrest, growth of Crack 3 resumed at the interface of E, via Branch 1. Later, Branch 2 would also start at the interface of E.

Before reaching its arrest point, Branch 1 traversed the interface of a transformed RA grain (A in Fig. 11***(a)***). Then, the crack propagated at an angle of ~75° to the load applied to arrest at another transformed RA grain (B in Fig. 11***(a)***). B was elongated and its major axis was roughly normal to the preferential growth direction. Crack path in AB followed the (1 1 0) slip plane of the martensite grain (Fig. 11***(b)***), for which the (1 1 0) [1–1–1] slip system had SF ≈ 0.45. Crack growth resumed by another branch, starting at C and again forming ~75° to the tensile load (Fig. 11***(a)***). This inclination was also consistent with a (1 1 0) slip plane, as the martensite grain was the same as in AB. Afterwards, the crack followed a zigzag, sequentially deflecting at the interfaces of transformed RA grains D and E (Fig. 12). In front of D, the zigzag occurred through a micro-crack formed between the crack path in AB, and D (Fig. 12). E fully transformed into martensite, but only the portions of D furthest and closest from the crack did (Fig. 11***(b)***). After E, Branch 1 continued at ~50° to the load applied. Branch 1 finally arrested at a relatively small, transformed RA grain (F in Fig. 11***(a)***), in front of which a minor deflection occurred (Fig. 12).

Regarding Branch 2, its final arrest point was a cluster of transformed RA grains (B in Fig. 13***(a)***). Multiple sub-branches ended at different parts of the interface of B. About Branch 3, its path started normal to the load applied (A in Fig. 13***(a)***), then formed a secondary micro-crack towards a transformed RA grain (C in Fig. 13***(a)***). Branch 3 continued along the preferential direction, then formed a strong zigzag, successively passing by two further transformed RA grains (D and E in Fig. 13 ***(a)***). Later, Branch 3 resumed the preferential growth direction up to its

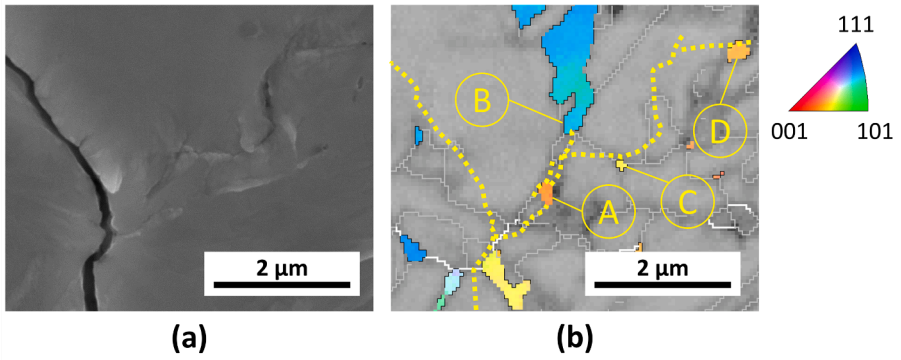

Fig.8. Segment of Crack 3 in an area rich in retained austenite: (a) SEM image and (b) EBSD map in the same area before testing. The dotted yellow line indicates the path followed by the crack. (For interpretation of the references to colour in this figure legend, the reader is referred to the web version of this article.)

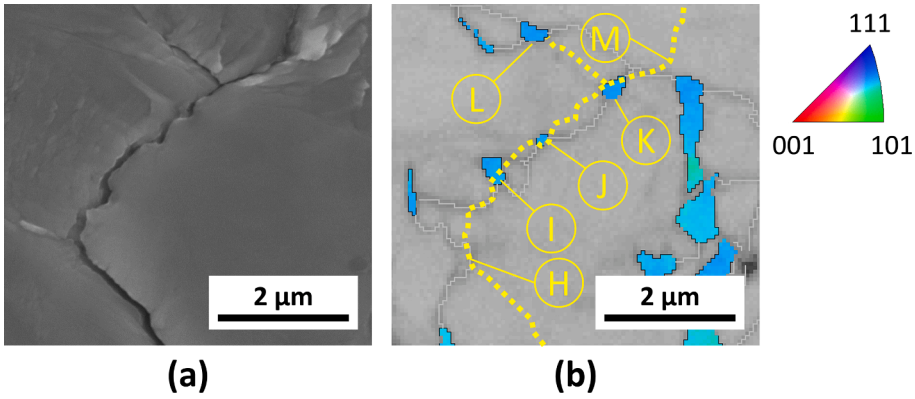

Fig.9. Segment of Crack 3 following a martensite boundary decorated with retained austenite: (a) SEM image and (b) EBSD map in the same area before testing. The dotted yellow line indicates the path followed by the crack. (For interpretation of the references to colour in this figure legend, the reader is referred to the web version of this article.)

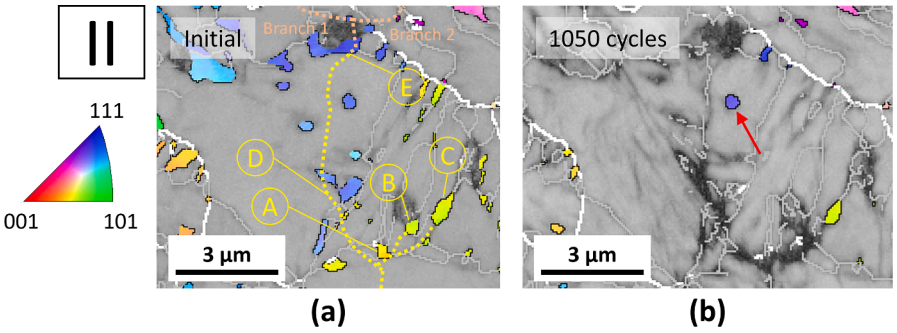

Fig.10. Area II of Crack 3: EBSD maps of the same area (a) before testing and (b) after 1050 cycles. The dotted yellow and orange lines indicate crack path before and after 1050 cycles. (For interpretation of the references to colour in this figure legend, the reader is referred to the web version of this article.)

final point after 1650 cycles. A transformed RA grain (F in Fig. 13***(a)***) lied in front of crack tip, but had not been reached yet.

3.3. Film-like retained austenite (RA) and crack growth

The size of the grains that could be resolved by EBSD was limited to a thickness of ~110 nm. However, grains with thickness smaller than 100 nm (commonly referred to as film-like RA) have been reported in Q&P steels [43,44]. Therefore, TEM analysis was performed to obtain information on the behavior of film-like RA. For this aim, a TEM sample was obtained around Crack 3 in the position indicated in Fig. 6***(a)***. This corresponded to a section of relatively quick growth along the preferential direction, within Subset II.

An overview of the sample is given in Fig. 14***(a)***, including the selected-area diffraction pattern of the region inside the red circle. The dark-field micrograph in Fig. 14***(c)*** corresponds to the diffraction spot highlighted with a red arrow in Fig. 14***(a)*** ((022) reflection in austenite). The figure demonstrates that relatively small RA grains were effectively observed in such region around the crack. These were untransformed, even if one of them (thickness ≈ 60 nm) was traversed by the crack (yellow arrow in Fig. 14***(b)***). The other one (thickness ≈ 100 nm) lied very close to the crack (distance ≈ 50 nm), but not on its path. There was no sign of deflection around neither of the two grains, or a branch growing towards that outside crack path. Moreover, no noticeable crack arrest occurred in this region (Fig. 6***(b)***).

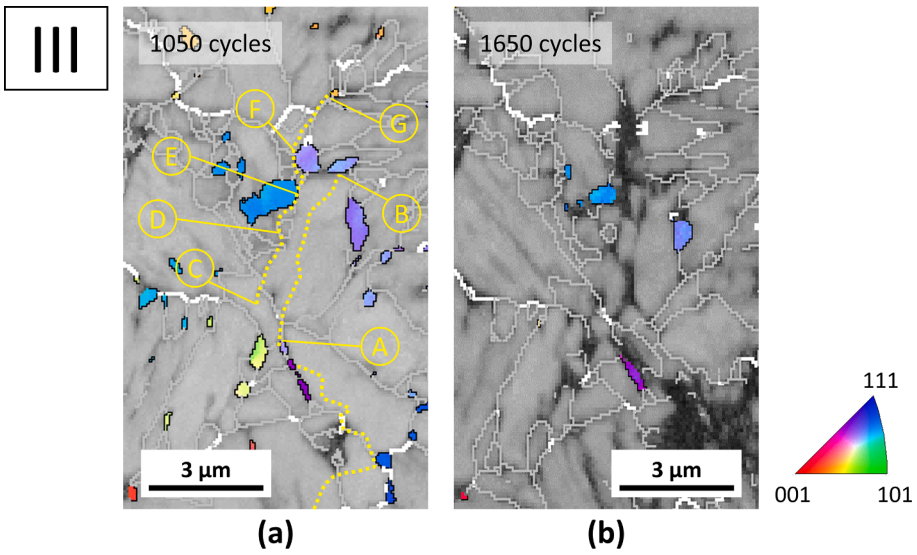

Fig.11. Area III of Crack 3: EBSD maps of the same area after (a) 1050 cycles and (b) 1650 cycles. The dotted yellow line indicates crack path. The purple lines account for slip plane traces, for which the slip system of highest Schmid factor (SF) is given. (For interpretation of the references to colour in this figure legend, the reader is referred to the web version of this article.)

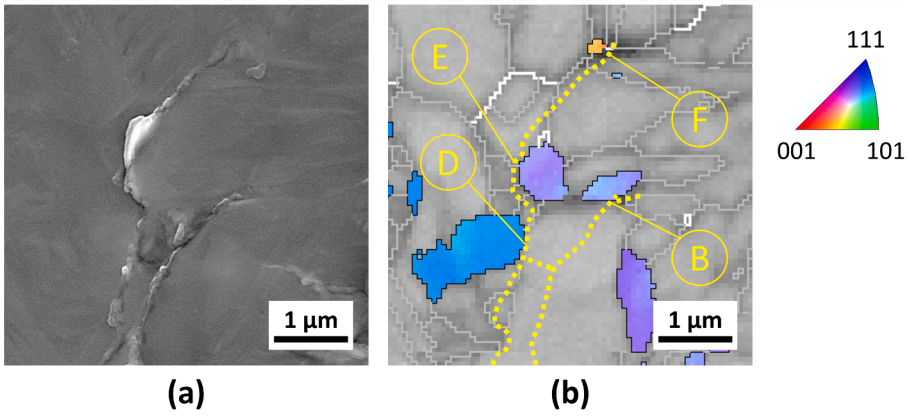

Fig.12. Segment of Crack 3 (Branch 1) describing a zigzag to follow retained austenite: (a) SEM image and (b) EBSD map in the same area before testing. The dotted yellow line indicates the path followed by the crack. (For interpretation of the references to colour in this figure legend, the reader is referred to the web version of this article.)

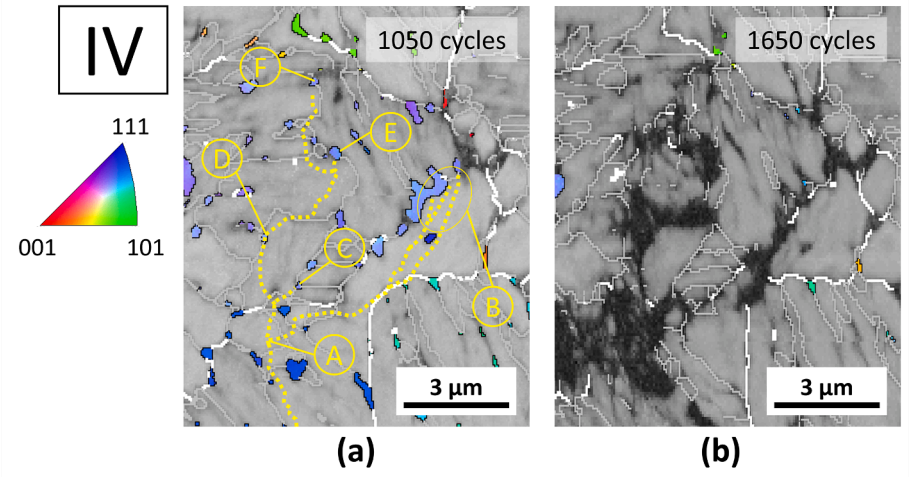

Fig.13. Area IV of Crack 3: EBSD maps of the same area after (a) 1050 cycles and (b) 1650 cycles. The dotted yellow line indicates crack path. (For interpretation of the references to colour in this figure legend, the reader is referred to the web version of this article.)

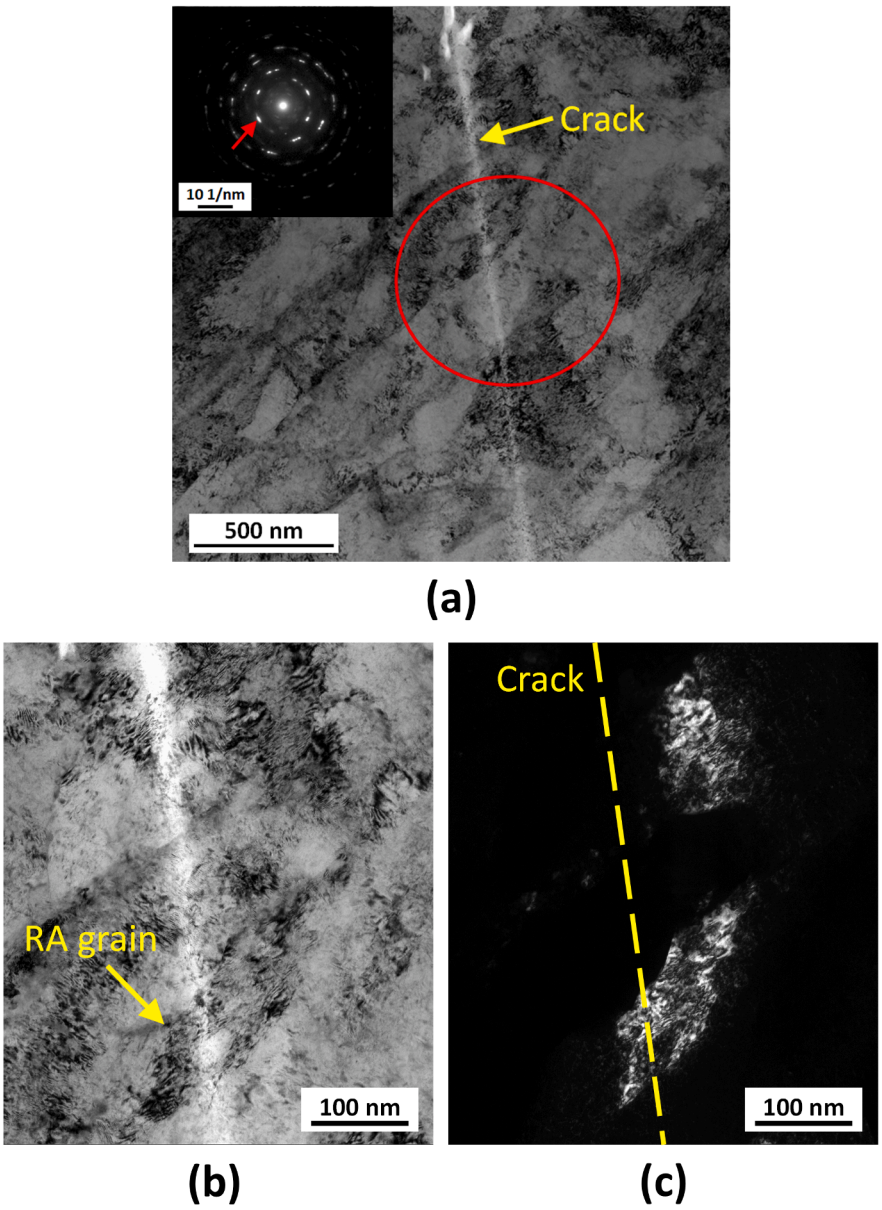

Fig.14. TEM image of Crack 3: (a) overview and (b,c) enlarged detail of the area in the red circle in (a). The diffraction pattern in (a) corresponds to the area in the red circle. (For interpretation of the references to colour in this figure legend, the reader is referred to the web version of this article.)

4. Discussion

The results above indicate that the majority of RA in the microstructure transforms into martensite ahead of short fatigue crack tip. They also show far-reaching interactions between this transformation and the paths and rates of the short crack growth. These are discussed below, together with recommendations for the design of second-phase RA microstructures resisting early fatigue crack growth.

4.1. Crack retardation by transformation-induced crack closure (TICC)

The most obvious retardation effect observed for the transformation of RA was the partial arrest of Crack 3 in subset II. This arrest can be explained by transformation-induced crack closure (TICC). Crack growth along the preferential direction was interrupted when the crack tip impinged the interface of transformed RA grain E (Fig. 10***(a)***). This grain had transformed ahead of the crack tip, as it was approached by the crack. When the tip reached its interface, the area would have thus been under the effect of the volume expansion due to the transformation. The resultant stress relaxation seems to have been strong enough to practically eliminate the driving force for any further propagation, at least for certain number of cycles. Therefore, the present study provides, for the first time, direct evidence of fatigue crack arrest by TICC due to second-phase RA transformation.

4.2. Crack retardation by roughness-induced crack closure (RICC)

Small-amplitude deflections consistently appeared in front of transformed RA grains. One example is the zigzag of Branch 1 just before its final arrest (DE in Fig. 12), produced by the crack following the interfaces of two closely spaced, transformed RA grains. Other examples can be seen at grains E in Fig. 4***(a)***, and D and E in Fig. 10***(a)***. Boundaries between martensite grains (e.g., A-D in Fig. 4***(a)***) also produced changes of direction. All these deflections gave rise to tortuous paths, which

assist crack retardation by roughness-induced crack closure (RICC). In RICC, misfit between the fracture surfaces of rough cracks leads to friction upon cyclic loading, reducing the local stress around the tip [23]. RICC by martensite hierarchical boundaries had been reported before [22,28]. Yet, the present study shows that second-phase RA transformation ahead of the crack also produces RICC. In fact, in the cracks studied, RA transformation led to stronger deflections (e.g., DE in Fig. 12). Moreover, the relatively strong zigzag of Branch 1 close to its final point suggests an important role of RICC in its arrest.

4.3. Crack retardation by crack deflection and branching

Crack growth often changed direction to follow transformed RA grains. Sometimes, cracks deviated so much as to become nearly parallel to the load applied, which is energetically unfavorable [42,45,46]. This occurred for Crack 2 (BC in Fig. 5***(b)***) and the Secondary Branch of Crack 3 (CE in Fig. 7***(a)***), and can partly explain their arrest. TICC at the transformed RA grains where the cracks stopped (C for Crack 2 and E/F for the Secondary Branch) should also have contributed. Yet, Crack 1 crossed a transformed RA grain while growing along the preferential direction (E in Fig. 4***(a)***), and TICC did not result in noticeable arrest. This suggests that TICC alone is often insufficient to interrupt crack growth. By contrast, concomitant deflection towards an unfavorable direction increases the chance of arrest. In addition, the tendency of cracks to follow transformed RA grains often resulted in strong zigzag paths. This happened e.g. for the Secondary Crack (BD in Fig. 8) and Branch 3 (DF in Fig. 13***(a)***). Such paths also collaborate in crack retardation by means of RICC, as explained in ***Section 4.2***.

Apart from this, cracks developed abundant branches. Moreover, relatively long branches recurrently sub-divided into shorter sub-branches. This includes the various sub-branches at the end of Branch 2 (B in Fig. 13***(a)***), and sub-branches developed during propagation of the main branches (e.g., BD in Fig. 5***(a)***, KL in Fig. 9, AB and AC in Fig. 10***(a)***, and C in Fig. 13***(a)***). All branches/sub-branches analyzed here directed towards transformed RA. This suggests that also the branching was driven by a tendency of cracks to follow RA. TICC once a transformed RA grain was reached should have also contributed by making any further propagation more favorable through an alternative branch. Branch development during crack growth reduces the rate of propagation by consuming additional energy and reducing stress localization, compared to a single crack path [24,29,45,47]. Hence, branching adds to TICC, RICC and crack deflection as the mechanisms whereby second-phase RA transformation retards short fatigue crack growth. The occurrence of independent secondary cracks following transformed RA (e.g., Crack 2) can be seen as analogous to branching.

The relative importance of crack deflection/branching and TICC without deflection/branching can be compared examining the growth rates of the cracks analyzed. For example, formation of Branch 2 meant no overall growth of Crack 3 for ~500 cycles: Branch 2 appeared at a less advanced position than Branch 1 had reached (Fig. 6***(b)***). Similarly, formation of Crack 2, and its arrest via deflection, interrupted the growth of Crack 1 (which led to specimen failure) for ~300 cycles (Fig. 13***(b)***). On the other hand, TICC without deflection or branching led at most to a partial arrest for ~150 cycles (subset II of Crack 3, Fig. 6***(b)***). This means that deflection and branching had a stronger retardation effect than TICC alone. The stronger retardation effect of deflection/branching also explains the slower growth of Crack 3 for 750–900 and 1150–1450 cycles (when branching/deflections occurred due to RA), compared to 900–1000 cycles (when crack path was essentially straight).

4.4. The interaction between retained austenite (RA) and short fatigue crack growth

The underlying reason for the crack deflection/branching observed is a tendency for short fatigue cracks to grow towards transformed RA. This is at odds with any expectation: short fatigue crack growth has been reported to occur normal to the stress applied [42], following microstructural boundaries [28,41,48], or along slip planes with high resolved shear stresses [28,41,48,49]. Yet, cracks here often deviated towards RA along directions not corresponding to any of these. Such deviations happened both when propagation was normal to the stress applied (e.g., AB in Fig. 5***(b)*** and DE in Fig. 13***(a)***), and along an active slip plane (e.g., H in Fig. 7***(a)***). This suggests a stronger tendency for short fatigue cracks to grow towards transformed RA than according to either option. Likewise, greater tendency compared to growth along microstructural boundaries is illustrated by the path not being the boundary itself, when cracks crossed several RA grains sitting along a single martensite boundary (e.g., BC in Fig. 5***(b)*** and IK in Fig. 9***(b)***).

An explanation to this unexpected behavior lies in the product of the RA transformation. In steels with second-phase RA, fresh martensite is typically much harder than the matrix [50,51]. This includes the tempered martensite matrix of Q&P steels [52]. First, fresh martensite has higher carbon content than tempered martensite due to the partitioning of carbon atoms. Second, partitioning results in partial softening of the martensitic matrix [53]. Such difference in hardness can result in strain incompatibility between transformed RA and the matrix. In turn, this can lead to interface decohesion [47], or strain localization and subsequent void/micro-crack generation around the fresh martensite [13].

The mechanism whereby the brittle character of fresh martensite can lead to crack deflection/branching is illustrated in Fig. 15. When transformed RA grains lie too far from the crack, the crack path simply follows the preferential growth direction (Fig. 15***(a)***). RA grains transform into fresh martensite once they become inside the plastic zone (Fig. 15***(b)***). This fresh martensite then acts as a brittle point in the microstructure. Hence, damage is induced around it by strain accumulation in the cycles after the transformation (Fig. 15***(c)***). Eventually, the main crack can grow towards the transformed RA grain by coalescence. If the RA grain was not aligned with crack tip along the preferential growth direction, the crack will deflect (Fig. 15***(d)***). TICC (and RICC) when the crack reaches the transformed RA will tend to arrest the branch. A new branch may then form, if another transformed RA grain exists in the plastic zone (Fig. 15***(e)***). Presence of several RA grains in the plastic zone at the same time can extend the amplitude of the deflection, by sequential growth towards them (Fig. 15***(f)***). In this sense, a recent *in situ* SEM study in a nickel superalloy showed a similar attraction of fatigue cracks to other brittle points in the microstructure, such as carbides and micro-pores [49]. As in the present case, crack branching and deflection resulted from the attraction, and led to slower crack growth [49]. The brittleness of fresh martensite can also explain the short-range deflections in front of transformed RA: the crack will grow towards the part of the interface most affected by decohesion or strain localization.

The mechanism for crack deflection/branching revealed here differs from that proposed by Huo and Gao [29], also for LCF. These authors suggested that crack deflection would occur when the crack spontaneously encountered a transformed RA grain. Due to the resultant TICC, crack growth could only resume by a new branch, inclined to the main crack [29]. By contrast, the present results show that crack deflections appear because cracks are actively attracted to transformed RA grains outside their natural path (even if TICC may facilitate the formation of new branches by hindering the growth of already formed ones). In fact, when Crack 3 precisely arrested by TICC, no significant deflection (or new branch) formed (E in Fig. 10***(a)***). On the contrary, crack growth just continued across the transformed RA, along the preferential direction. This was likely also related to the brittle character of fresh martensite: if voids/micro-cracks formed at the interface and inside the transformed RA grain in the cycles of the arrest, the crack would have eventually grown across it by coalescence.

Additionally, the mechanism presented here for crack deflection/branching can explain former results on fatigue crack propagation in

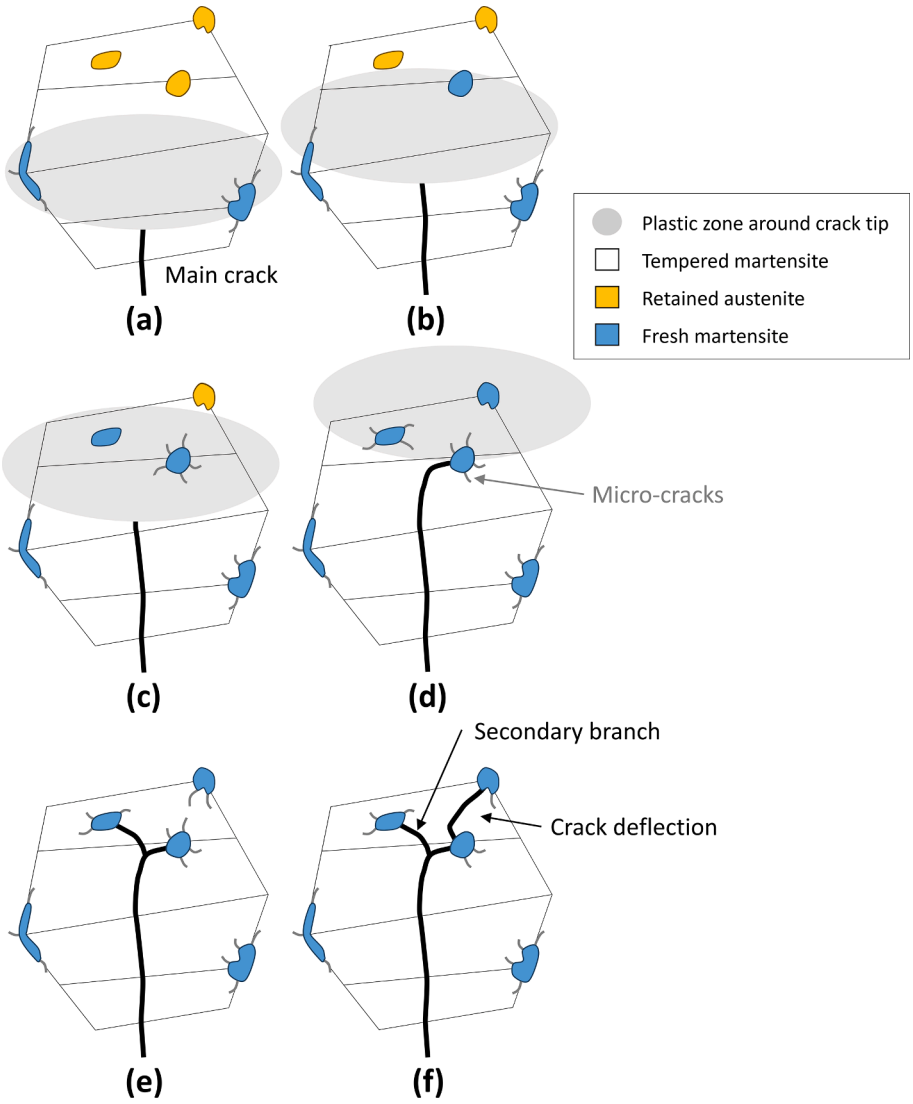

Fig.15. Mechanism of crack branching and deflection induced by the transformation of second-phase retained austenite.

steels including second-phase RA. For instance, Zhou *et al.* reported more deflections/branching in the CFB steel that exhibited the most RA transformation during LCF [13,18]. Similarly, Song *et al.* observed more deflections/branches in a TRIP grade under HCF than for two other RA-containing steels, which underwent less RA transformation [47]. In both studies, the material with more deflections and branching reached longer fatigue life [13,18,47]. Yet, neither associated the effect with the greater RA transformation, which our study makes possible. Moreover, the similar observations of deflection/branching under LCF and HCF suggest that the mechanism proposed applies regardless of the level of cyclic stress imparted.

Finally, the profuse existence of fresh martensite ahead of crack tip (as most RA available transforms) could be thought to be detrimental by providing a quick path for crack growth [14,24]. However, this seems counteracted by the considerable number of new branches and deflections: the transformation of second-phase RA ahead of short fatigue cracks creates a constellation of brittle points, which produce a complex panorama of secondary cracks, branches, and deflections towards them. Together with TICC and RICC when cracks/branches impinge the transformed RA grains, this leads to abundant extra energy consumed, and an overall retardation of short fatigue crack growth. The results presented correspond to two specimens and three cracks, for a combined short crack length studied of > 90 μm. Nevertheless, the mechanisms of the interaction between RA and the short cracks were the same for all regions and specimens. This means that the sampling size was sufficient for the mechanisms to be fully clarified.

4.5. Design of retained-austenite (RA) microstructures for crack retardation

The mechanisms identified in the previous sections allow extracting recommendations for the design of second-phase RA microstructures to delay short fatigue crack growth. In this sense, our work focused on one material and loading condition only (i.e. LCF). Nevertheless, as noted above, the relationship between RA transformation and crack deflection/branching (and their beneficial effect on fatigue) has been consistently found in studies on steel types other than Q&P, under both LCF and HCF [13,18,38,47]. This means that, on the one hand, recommendations below are expected to apply to the various multi-phase steel types comprising second-phase RA. Yet, it should be noted that the studies considered do not cover all the range of possible steel microstructures with second-phase RA. For example, RA volume fraction (as measured by XRD) is limited to 10–15 % in all cases. Likewise, average RA grain sizes are always within 0.2–0.5 μm [13,18,38,47]. For higher RA fraction or different RA size, the crack deflection and branching owing to RA transformation may affect fatigue performance differently.

However, even for such cases, this study provides a framework to assess the effect of RA transformation, by clarifying the mechanism of its interaction with short fatigue cracks. On the other hand, for HCF [13,18,38,47], the recommendations below should also directly apply, as an even greater effect of the deflection/branching due to RA transformation would be expected. This is due to the lower tendency of cracks to follow the preferential growth direction, according to lower stress intensity factor [42].

Firstly, the different behavior of Cracks 1 and 2 highlights the importance of high RA volume fractions in each PAG: growth of Crack 2 through a RA-rich PAG resulted in its arrest via deflection/branching. By contrast, Crack 1 grew uninterruptedly across a RA-lean PAG.

Secondly, Crack 2 speaks also of the role of RA grain inclination with respect to crack path: Crack 2 deflected by interaction with an elongated RA grain, with major axis normal to the preferential growth direction. By contrast, it had grown uninterruptedly through the previous PAG, whose RA grains were also elongated, but parallel to that direction. Obviously, the chance that a RA grain lies in the path of the crack (and thus interacts with it) increases with larger area normal to growth. For the same size, a RA grain is thus more beneficial the higher its aspect ratio, and the greater the inclination of its major axis to the growth direction. This is confirmed by Table 3: the RA grains behind the main retardation events observed had all aspect ratios higher than ~2.3 (while such RA grains accounted for only ~40 % of those in the initial microstructure). Moreover, the inclination of their major axes to the preferential growth direction was always at least ~60°, except for the RA grain where Branch 2 arrested. For the RA grains behind the partial arrest of Crack 3 and the deflection of Crack 2, inclination even exceeded ~80°. Only ~30 % and ~12 % of the initial RA grains were inclined more than 60° and 80°, respectively.

Similarly, with the exception of the deflection of Crack 2, all main retardation events involved a RA grain larger than ~0.80 μm (Table 3). Less than 2 % of initial RA grains were in such size range. Larger RA size could be thought to increase the size incompatibility between fresh martensite and matrix. This would increase the extent of the damage via voids/microcracks, enhancing the "attractive" effect of RA and the deflection/branching/RICC. The stress relaxation around the fresh martensite would also be enhanced, increasing the chances of crack arrest by TICC. Larger RA grain size would thus explain why crack arrest via TICC occurred for Crack 3 in Subset II (Table 3), but not for grain E of Crack 1, both encountered without retardation mechanisms other than TICC (Table 4). Crack 2 and Branch 1 ended at relatively small RA grains, but mechanisms additional to TICC were active (Table 4). Our results indicate thus that larger RA grain sizes and aspect ratios are more effective to retard short fatigue cracks. However, due to the limited number of retardation events in Table 3 and Table 4, attention should be paid to the qualitative trend, rather than the specific sizes/aspect ratios (e.g., 0.8 μm and 2.3).

About RA stability, RA grains untransformed upon crack passage do not contribute to crack retardation. Some examples are the film-like RA shown by TEM, and the RA grain highlighted in Fig. 10***(a)***. None of these caused noticeable arrest, deflection, or branching. In particular, the lack of transformation of film-like RA can be explained by its small grain size, widely known to preclude RA transformation [3,18,54,55]. Nevertheless, this is in contrast with Gao *et al.*, who did find film-like fresh martensite at the tip of a non-propagating crack [14]. Furthermore, the study focused on HCF [14], so that lower driving force for transformation than in the present experiments would be expected. In this sense, occurrence of transformation for Gao *et al.* as opposed to this case can be attributed to softer matrix in their material, a CFB steel [14]. Harder surrounding phases can hinder RA transformation by exerting hydrostatic stresses against the volume expansion associated [3,37,56,57]. This explanation is supported by other studies: Huo and Gao observed film-like fresh martensite around a LCF crack in a steel with ferrite matrix (relatively soft) [29], but Qi *et al.* found untransformed film-like RA near a HCF crack in a steel with martensite matrix (relatively hard) [24]. Additionally, the lack of contribution of untransformed RA to crack retardation can explain the effect of RA stability on fatigue as reported in the literature. For similar initial RA fraction, Song *et al.* found longer HCF life for the material with most unstable RA [47]. This was the only material studied exhibiting significant RA transformation [47]. Similarly, fatigue life reductions in chemical compositions and heat treatments leading to higher RA stability have also been reported by other authors [19,58]. In this sense, if RA is too stable to transform within the plastic zone, the retarding mechanisms due to RA will not be activated.

In conclusion, this study suggests that retardation of short fatigue crack growth benefits from higher RA volume fractions. RA should be evenly distributed across all PAGs, to avoid weaker areas prone to fatigue. RA grains should also have the degree of stability to transform in the plastic zone around crack tip. Finally, RA grains with relatively large size, high aspect ratio and major axis parallel to the principal tensile stress (i.e. normal to the preferential growth direction) should be promoted. This can be done by adjusting the conventional thermo-mechanical processing of multi-phase steels, but also with recently-developed localized laser treatments [36,37]. In fact, recent work with those treatments has proved that RA grains with high aspect ratio and parallel to the tensile stress also improve ductility and uniform elongation in monotonic testing [37]. This would extend the benefit of such RA grains beyond fatigue.

5. Conclusions

The effect of RA as a second phase on short fatigue crack growth has been examined for a Q&P steel, via quasi *in situ* EBSD characterization and TEM analysis. These are the main conclusions of the study:

Table 3
Quantitative description of the retained austenite grains behind the main crack retardation events.

RA Grain	Diameter (μm)	Aspect Ratio	Inclination to Crack Growth Direction (°)	Retarding Mechanism
B (Crack 2)	0.33	2.41	80.5	Deflection
E (Crack 3 – Subset II)	0.82	3.15	88.9	TICC
D (Branch 1 – Subset III)	0.93	2.27	62.4	RICC
E (Branch 1 – Subset III)	0.43	2.60	69.8	RICC
B (Branch 2 – Subset IV)	0.97	2.31	36.9	TICC

Table 4
Quantitative description of the retained austenite grains where different cracks terminated by TICC.

RA Grain	Diameter (μm)	Aspect Ratio	Inclination to Crack Growth Direction (°)	Mechanism Added to TICC
E (Crack 1)	0.30	1.58	77.9	None
C (Crack 2)	0.26	2.52	38.0	Deflection
F (Branch 1 – Subset III)	0.19	1.39	20.3	RICC

1. The strain induced by the plastic zone ahead of short fatigue crack tip transforms most of the RA inside the plastic zone into martensite. The smallest RA grains represent an exception, on account of their higher mechanical stability.
2. Short fatigue crack growth frequently occurs towards transformed RA. This unexpected effect has been related to the brittle character of the resultant fresh martensite. Attraction of cracks to transformed RA is stronger than their tendency to grow perpendicularly to the principal tensile stress, along crystallographic planes with high Schmid factors, or microstructural boundaries.
3. Transformation of RA into martensite ahead of crack tip delays short crack growth, and can result in the definitive arrest of short cracks. The retardation/arrest occurs by a combination of mechanisms due to the RA transformation: crack deflection towards unfavorable directions, branching, RICC and TICC. Crack deflection, branching and RICC are driven by the tendency of cracks to grow towards transformed RA, not reported in former literature. Crack deflection and branching are more powerful than TICC acting alone in delaying short crack growth.
4. Relatively large RA grains, with high aspect ratio and major axis parallel to the principal tensile stress are most effective in delaying short fatigue crack growth. Microstructures comprising second-phase RA should avoid RA-lean PAGs, and RA not transforming ahead of the crack.

CRediT authorship contribution statement

Pablo Garcia-Chao: Writing – review & editing, Writing – original draft, Visualization, Investigation, Data curation, Conceptualization. **Jon M. Molina-Aldareguia:** Writing – review & editing, Resources, Funding acquisition, Conceptualization. **Bernd M. Linke:** Writing – review & editing, Resources. **Richard G. Thiessen:** Writing – review & editing, Resources. **Ilchat Sabirov:** Writing – review & editing, Supervision, Resources, Funding acquisition, Conceptualization.

Declaration of competing interest

The authors declare that they have no known competing financial interests or personal relationships that could have appeared to influence the work reported in this paper.

Data availability

Data will be made available on request.

Acknowledgements

This work was financially supported by the Research Fund for Coal and Steel (RFCS) via the project OptiQPAP [Grant Agreement Number: 709755]. The authors also thank Dr. Miguel Castillo-Rodriguez for help with FIB sample preparation and TEM characterization.

References

[1] Z. Dai, H. Chen, R. Ding, Q. Lu, C. Zhang, Z. Yang, S. van der Zwaag, Fundamentals and application of solid-state phase transformations for advanced high strength steels containing metastable retained austenite, Mater. Sci. Eng. R 143 (2021) 100590.
[2] WorldSteelAssociation, Advanced high-strength steels (AHSSs) Application Guidelines Version 7.0, 2021.
[3] E.V. Pereloma, A.A. Gazder, I.B. Timokhina, Retained austenite: transformation-induced plasticity, in: R. Colas, G.E. Totten (Eds.), Encyclopedia of Iron, Steel, and Their Alloys, CRC Press, New York, 2016, pp. 3088–3103.
[4] C.B. Finfrock, A.J. Clarke, G.A. Thomas, K.D. Clarke, Austenite stability and strain hardening in C-Mn-Si quenching and partitioning steels, Metall. Mater. Trans. A 51 (2020) 2025–2034.
[5] T. Yokoi, K. Kawasaki, M. Takahashi, K. Koyama, M. Mizui, Fatigue properties of high strength steels containing retained austenite, Int. J. Fatigue 8 (19) (1997) 662.
[6] M. Abareshi, E. Emadoddin, Effect of retained austenite characteristics on fatigue behavior and tensile properties of transformation induced plasticity steel, Mater. Des. 32 (10) (2011) 5099–5105.
[7] Z.G. Hu, P. Zhu, J. Meng, Fatigue properties of transformation-induced plasticity and dual-phase steels for auto-body lightweight: experiment, modeling and application, Mater. Des. 31 (6) (2010) 2884–2890.
[8] G.N. Haidemenopoulos, A.T. Kermanidis, C. Malliaros, H.H. Dickert, P. Kucharzyk, W. Bleck, On the effect of austenite stability on high cycle fatigue of TRIP 700 steel, Mater. Sci. Eng. A 573 (2013) 7–11.
[9] P.I. Christodoulou, A.T. Kermanidis, D. Krizan, Fatigue behavior and retained austenite transformation of Al-containing TRIP steels, Int. J. Fatigue 91 (2016) 220–231.
[10] Z.Z. Hu, M.L. Ma, Y.Q. Liu, J.H. Liu, The effect of austenite on low cycle fatigue in three-phase steel, Int. J. Fatigue 19 (8–9) (1997) 641–646.
[11] N. Yoshikawa, J. Kobayashi, K. Sugimoto, Notch-fatigue properties of advanced TRIP-aided bainitic ferrite steels, Metall. Mater. Trans. A 43 (2012) 4129–4136.
[12] P. Ostermayer, T. Allam, X. Shen, W. Song, K. Burkart, B. Blinn, B. Clausen, W. Bleck, T. Beck, Effect of retained austenite on the fatigue behavior of modified bainitic 100Cr6 steels considering local phase transformation, Mater. Sci. Eng. A 877 (2023) 145204.
[13] Q. Zhou, L. Qian, J. Meng, L. Zhao, The fatigue properties, microstructural evolution and crack behaviors of low-carbon carbide-free bainitic steel during low-cycle fatigue, Mater. Sci. Eng. A 820 (2021) 141571.
[14] G. Gao, R. Liu, K. Wang, X. Gui, R.D.K. Misra, B. Bai, Role of retained austenite with different morphologies on sub-surface fatigue crack initiation in advanced bainitic steels, Scr. Mater. 184 (2020) 12–18.
[15] X. Long, F. Zhang, Z. Yang, B. Lv, Study on microstructures and properties of carbide-free and carbide-bearing bainitic steels, Mater. Sci. Eng. A 715 (2018) 10–16.
[16] X. Feng, F. Zhang, J. Kang, Z. Yang, X. Long, Sliding wear and low cycle fatigue properties of new carbide free bainitic rail steel, Mater. Sci. Technol. 30 (12) (2014) 1410–1418.
[17] F. Zhang, X. Long, J. Kang, D. Cao, B. Lv, Cyclic deformation behaviors of a high strength carbide-free bainitic steel, Mater. Des. 94 (2016) 1–8.
[18] Q. Zhou, L. Qian, J. Meng, L. Zhao, F. Zhang, Low-cycle fatigue behavior and microstructural evolution in a low-carbon carbide-free bainitic steel, Mater. Des. 85 (2015) 487–496.
[19] P. Ostermayer, B. Blinn, U. Krupp, T. Beck, VHCF behavior and defect tolerance of modified bainitic 100Cr6 with a high retained austenite content, Int. J. Fatigue 108378 (2024).
[20] I. Černy, D. Mikulova, J. Sis, B. Mašek, H. Jirkova, J. Malina, Fatigue properties of a low alloy 42SiCr steel heat treated by quenching and partitioning process, Procedia Eng. 10 (2011) 3310–3315.
[21] I. de Diego-Calderón, P. Rodriguez-Calvillo, A. Lara, J.M. Molina-Aldareguia, R. H. Petrov, D. De Knijf, I. Sabirov, Effect of microstructure on fatigue behavior of advanced high strength steels produced by quenching and partitioning and the role of retained austenite, Mater. Sci. Eng. A 641 (2015) 215–224.
[22] A. Sierra-Soraluce, G. Li, M.J. Santofimia, J.M. Molina-Aldareguia, A. Smith, M. Muratori, I. Sabirov, Exploring the effect of complex hierarchic microstructure of quenched and partitioned martensitic stainless steels on their high cycle fatigue behaviour, Mater. Des. 233 (2023) 112286.
[23] M. Koyama, Z. Zhang, M. Wang, D. Ponge, D. Raabe, K. Tsuzaki, H. Noguchi, C. C. Tasan, Bone-like crack resistance in hierarchical metastable nanolaminate steels, Science 355 (6329) (2017) 1055–1057.
[24] X.Y. Qi, L.X. Du, J. Hu, R.D.K. Misra, High-cycle fatigue behavior of low-C medium-Mn high strength steel with austenite-martensite submicron-sized lath-like structure, Mater. Sci. Eng. A 718 (2018) 477–482.
[25] Y.-B. Ju, M. Koyama, T. Sawaguchi, K. Tsuzaki, H. Noguchi, In situ microscopic observations of low-cycle fatigue-crack propagation in high-Mn austenitic alloys with deformation-induced ε-martensitic transformation, Acta Mater. 112 (2016) 326–336.
[26] M. Zhang, W. Wang, B. Zhang, Q. Cen, J. Liu, Influence of pre-straining on the low-cycle fatigue performance of Fe–0.1 C–5Mn medium manganese steel, Int. J. Fatigue 165 (2022) 107186.
[28] Z. Zhang, M. Koyama, M.M. Wang, K. Tsuzaki, C.C. Tasan, H. Noguchi, Microstructural mechanisms of fatigue crack non-propagation in TRIP-maraging steels, Int. J. Fatigue 113 (2018) 126–136.
[29] C.Y. Huo, H.L. Gao, Strain-induced martensitic transformation in fatigue crack tip zone for a high strength steel, Mater Charact. 55 (1) (2005) 12–18.
[30] X. Cheng, R. Petrov, L. Zhao, M. Janssen, Fatigue crack growth in TRIP steel under positive R-ratios, Eng. Fract. Mech. 75 (3–4) (2008) 739–749.
[31] G. Gao, B. Zhang, C. Cheng, P. Zhao, H. Zhang, B. Bai, Very high cycle fatigue behaviors of bainite/martensite multiphase steel treated by quenching-partitioning-tempering process, Int. J. Fatigue 92 (2016) 203–210.
[32] U. Krupp, C. West, H.-J. Christ, Deformation-induced martensite formation during cyclic deformation of metastable austenitic steel: Influence of temperature and carbon content, Mater. Sci. Eng. A 481 (2008) 713–717.
[33] M. Kumagai, M. Kuroda, T. Matsuno, S. Harjo, K. Akita, In situ neutron diffraction analysis of microstructural evolution-dependent stress response in austenitic stainless steel under cyclic plastic deformation, Mater. Des. 221 (2022) 110965.
[34] D. De Knijf, R. Petrov, C. Föjer, L.A.I. Kestens, Effect of fresh martensite on the stability of retained austenite in quenching and partitioning steel, Mater. Sci. Eng. A 615 (2014) 107–115.
[35] K.J. Miller, The behaviour of short fatigue cracks and their initiation part ii-a general summary, Fatigue Fract. Eng. Mater. Struct. 10 (2) (1987) 93–113.

[36] H.J. Breukelman, M.J.M. Hermans, M.J. Santofimia, J. Hidalgo, Engineering austenite/martensite mesostructured materials by controlled localised laser treatments in a Fe–Ni–C alloy, Mater. Des. 227 (2023) 111772.
[37] H. Breukelman, M.J. Santofimia, J. Hidalgo, Hierarchically patterned multiphase steels created by localised laser treatments, Mater. Des. 221 (2022) 110984.
[38] P. Xia, F. Vercruysse, C. Celada-Casero, P. Verleysen, R.H. Petrov, I. Sabirov, J. M. Molina-Aldareguia, A. Smith, B. Linke, R. Thiessen, D. Frometa, S. Parareda, A. Lara, Effect of alloying and microstructure on formability of advanced high-strength steels processed via quenching and partitioning, Mater. Sci. Eng. A 831 (2022) 142217.
[39] W.-S. Li, H.-Y. Gao, H. Nakashima, S. Hata, W.-H. Tian, In-situ EBSD study of deformation behavior of retained austenite in a low-carbon quenching and partitioning steel via uniaxial tensile tests, Mater Charact 118 (2016) 431–437.
[40] N. Bernier, L. Bracke, L. Malet, S. Godet, An alternative to the crystallographic reconstruction of austenite in steels, Mater Charact 89 (2014) 23–32.
[41] I. Alvarez-Armas, U. Krupp, M. Balbi, S. Hereñú, M.C. Marinelli, H. Knobbe, Growth of short cracks during low and high cycle fatigue in a duplex stainless steel, Int. J. Fatigue 41 (2012) 95–100.
[42] G.E. Dieter, Mechanical Metallurgy, McGraw-Hill Book Company, London, 1988.
[43] X.C. Xiong, B. Chen, M.X. Huang, J.F. Wang, L. Wang, The effect of morphology on the stability of retained austenite in a quenched and partitioned steel, Scr. Mater. 68 (5) (2013) 321–324.
[44] F. Peng, Y. Xu, J. Li, X. Gu, X. Wang, Interaction of martensite and bainite transformations and its dependence on quenching temperature in intercritical quenching and partitioning steels, Mater. Des. 181 (2019) 107921.
[45] T.P. Bui, Y. Miyashita, Y. Mutoh, Y. Morikage, T. Tagawa, T. Handa, Y. Otsuka, Fatigue crack deflection and branching behavior of low carbon steel under mechanically large grain condition, Int. J. Fatigue 148 (2021) 106217.
[46] D.A. Lados, D. Apelian, J.F. Major, Fatigue crack growth mechanisms at the microstructure scale in Al-Si-Mg cast alloys: Mechanisms in regions II and III, Metall. Mater. Trans. A 37 (2006) 2405–2418.
[47] C. Song, H. Wang, Z. Sun, Z. Wei, H. Yu, H. Chen, Y. Wang, J. Lu, Effect of multiphase microstructure on fatigue crack propagation behavior in TRIP-assisted steels, Int. J. Fatigue 133 (2020) 105425.
[48] F. Briffod, A. Bleuset, T. Shiraiwa, M. Enoki, Effect of crystallographic orientation and geometrical compatibility on fatigue crack initiation and propagation in rolled Ti-6Al-4V alloy, Acta Mater. 177 (2019) 56–67.
[49] L. Zhang, L.G. Zhao, A. Roy, V.V. Silberschmidt, G. McColvin, In-situ SEM study of slip-controlled short-crack growth in single-crystal nickel superalloy, Mater. Sci. Eng. A 742 (2019) 564–572.
[50] X. Gu, Y. Xu, F. Peng, R.D.K. Misra, Y. Wang, Role of martensite/austenite constituents in novel ultra-high strength TRIP-assisted steels subjected to non-isothermal annealing, Mater. Sci. Eng. A 754 (2019) 318–329.
[51] M. Wang, M.X. Huang, Abnormal TRIP effect on the work hardening behavior of a quenching and partitioning steel at high strain rate, Acta Mater. 188 (2020) 551–559.
[52] I. de Diego-Calderón, D. De Knijf, M.A. Monclús, J.M. Molina-Aldareguia, I. Sabirov, C. Föjer, R.H. Petrov, Global and local deformation behavior and mechanical properties of individual phases in a quenched and partitioned steel, Mater. Sci. Eng. A 630 (2015) 27–35.
[53] J. Speer, D.K. Matlock, B.C. De Cooman, J.G. Schroth, Carbon partitioning into austenite after martensite transformation, Acta Mater. 51 (9) (2003) 2611–2622.
[54] D. De Knijf, C. Föjer, L.A.I. Kestens, R. Petrov, Factors influencing the austenite stability during tensile testing of Quenching and Partitioning steel determined via in-situ Electron Backscatter Diffraction, Mater. Sci. Eng. A 638 (2015) 219–227.
[55] D. Adams, M. Behling, M. Miles, E. Homer, A. Sachdev, E. White, D. Fullwood, Characterization of the factors influencing retained austenite stability in Q&P Steels via In Situ EBSD, Metall. Mater. Trans. A 54 (4) (2023) 1355–1363.
[56] C. Celada-Casero, B. Huang, J.-R. Yang, D. San-Martín, Microstructural mechanisms controlling the mechanical behaviour of ultrafine grained martensite/austenite microstructures in a metastable stainless steel, Mater. Des. 181 (2019) 107922.
[57] J. Kang, N.S. Pottore, H. Zhu, C.C. Tasan, An in situ investigation of neighborhood effects in a ferrite-containing quenching and partitioning steel: Mechanical stability, strain partitioning, and damage, Acta Mater. 254 (2023) 118985.
[58] D. Morris, F. Sadeghi, Retained austenite stability on rolling contact fatigue performance of 8620 case-carburized steel, Fatigue Fract. Eng. Mater. Struct. 45 (1) (2022) 55–68.

Further reading

[27] C. Zhang, Z. Xiong, D. Yang, X. Cheng, Heterogeneous quenching and partitioning from manganese-partitioned pearlite: retained austenite modification and formability improvement, Acta Mater. 235 (2022) 118060.